Article

Unsteady Water-Based Ternary Hybrid Nanofluids on Wedges by Bioconvection and Wall Stretching Velocity: Thermal Analysis and Scrutinization of Small and Larger Magnitudes of the Thermal Conductivity of Nanoparticles

Isaac Lare Animasaun [1,2,*], Qasem M. Al-Mdallal [2], Umair Khan [3,4] and Ali Saleh Alshomrani [5]

1 Fluid Dynamics and Survey Research Group, Department of Mathematical Sciences, Federal University of Technology, Akure PMB 704, Nigeria
2 Department of Mathematical Sciences, United Arab Emirates University, Al Ain, Abu Dhabi PMB 15551, United Arab Emirates
3 Department of Mathematical Sciences, Faculty of Science and Technology, Universiti Kebangsaan Malaysia, UKM, Bangi 43600, Selangor, Malaysia
4 Department of Mathematics and Social Sciences, Sukkur IBA University, Sukkur 65200, Sindh, Pakistan
5 Mathematical Modelling and Applied Computation (MMAC) Research Group, Department of Mathematics, Faculty of Science, King Abdulaziz University, P.O. Box 80203, Jeddah 21589, Saudi Arabia
* Correspondence: anizakph2007@gmail.com

Abstract: The uniqueness of nanofluids in the field of thermal analysis and engineering is associated with their thermal conductivity and thermodynamics. The dynamics of water made up of (i) single-walled carbon nanotubes with larger magnitudes of thermal conductivity of different shapes (i.e., platelet, cylindrical, and spherical) and (ii) moderately small magnitudes of thermal conductivity (i.e., platelet magnesium oxide, cylindrical aluminum oxide, spherical silicon dioxide) were explored in order to address some scientific questions. In continuation of the exploration and usefulness of ternary hybrid nanofluid in hydrodynamics and geothermal systems, nothing is known on the comparative analysis between the two dynamics outlined above due to the bioconvection of static wedges and wedges with stretching at the wall. Reliable and valid numerical solutions of the governing equation that models the transport phenomena mentioned above are presented in this report. The heat transfer through the wall increased with the wall stretching velocity at a smaller rate of 0.52 and a higher rate of 0.59 when the larger and smaller thermal conductivity of nanoparticles were used, respectively. Larger or smaller magnitudes of the thermal conductivity of nanoparticles were used; the wall stretching velocity had no significant effects on the mass transfer rate but the distribution of the gyrotactic microorganism was strongly affected. Increasing the stretching at the wedge's wall in the same direction as the transport phenomenon is suitable for decreasing the distribution of temperature owing to the higher velocity of ternary hybrid nanofluids either parallel or perpendicular to the wedge.

Keywords: ternary hybrid nanofluids; SWCNT nanoparticles; platelet magnesium oxide; cylindrical aluminum oxide nanoparticles; spherical silicon dioxide nanoparticles

MSC: 76R10; 76-10

1. Introduction

Experts dealing with microelectromechanical systems and nanoelectromechanical systems have expressed interest in single-walled carbon nanotubes because of their excellent electrical, structural, and mechanical capabilities, as proved by Baughman et al. [1]. Carbon nanotubes are excellent heat and cold conductors because of their outstanding thermal conductivity. Although silver and other metals are quite effective heat conductors, carbon

nanotubes have thermal conductivity that is ten times greater than silver. According to Kim et al. [2], Prasek et al. [3], Dai [4], Li et al. [5], and Zhang et al. [6], the length of the nanotube, magnitude of temperature, reliance on phonons instead of electrons, axial strain, interaction between the nanotube with the substrate, chirality, and radius of the tube are likely factors that could influence the thermal conductivity of SWCNTs. Yu-Hua et al. [7] showed that beyond 30 degrees Celsius, single-walled carbon nanotube-based nanofluids change in thermal conductivity significantly quicker than ordinary water. It was also suggested in the same report that the Brownian motion of the particles drives the rise in thermal conductivity with temperature.

Nanda et al. [8] contributed to the study on the colloidal mixture of (a) ethylene glycol and single-wall carbon nanotubes and (b) (poly)-alpha-olefins and single-wall carbon nanotubes with the primary purpose of emphasizing the relevance of the interfacial thermal boundary layer and its corresponding resistance. The experimental findings demonstrated that the suspension of a single-wall carbon nanotube increased the thermal conductivity of ethylene glycol and (poly)-alpha olefins. The exceptional chemical and thermal stabilities, good tensile strength, and light weight of water-conveying single-walled carbon nanotubes were validated by Sabiha et al. [9]. The stability and characteristics of ordinary water and water-conveying single-walled carbon nanotubes indicate that from 0.05 vol% and 20 degrees Celsius to 0.25 vol% and 60 degrees Celsius, the thermal conductivity of water increases from 2.84% to 36.39%. The stability and thermo–physicality of ordinary water and water-conveying single-walled carbon nanotubes indicate that from 0.05 vol% and 20 degrees Celsius to 0.25 vol% and 60 degrees Celsius, the thermal conductivity of water increases from 2.84% to 36.39%. Additionally, the findings demonstrate that the nanofluid's viscosity dynamic decreases while temperature increases. As a result, the specific heat of the fluids rose from 6.73 to 28.96% at 20 °C to 60 °C temperature and volume concentrations of 0.05–0.25 vol%. However, compared to water, nanofluids possess smaller specific heat capacities. The results mentioned above were also corroborated by the findings of Said [10] on the thermal conductivity of water-carrying single-walled carbon nanotubes at temperatures between 20 and 60 degrees Celsius and volume percentages between 0.10 and 0.50. Namarvari et al. [11] performed a molecular dynamics simulation of a colloidal water mixture with single-walled carbon nanotubes at 298 and 313 K to investigate the impact of volume fraction on the viscosity of the nanofluid. The findings show that viscosity increases due to a rise in volume fraction. Additionally, the results indicate that as temperature ascended, the viscosity of the same nanofluid reduced.

The efficiency of hydrodynamics, geothermal systems, nuclear waste storage, magnetohydrodynamics, thermal insulation, heat exchangers, and crude oil exploration and extraction are significantly influenced by thermal conductivity; see Alqahtani et al. [12], Sarkar and Endalew [13]. Experts researching these areas within the scope of science are all interested in understanding and exploring the dynamics of fluid substances colloidally mixed with tiny particles over wedge-shaped surfaces. The wedge angle is important for the exploration of transonic flows over airfoils and wings because it is difficult to eliminate the corner owing to a finite wedge angle at the trailing edge; Jameson [14]. The dynamics of viscous fluid starting from the sharp edge of the wedge were reviewed by Stewartson [15] and Riccardi and Iafrati [16]; horizontal surfaces of the paraboloid were reviewed by Makinde and Animasaun [17,18]. The velocity of the laminar flow in the vicinity of the apex was elucidated by Schlichting [19] as a variable that varied with the wedge angle and distance away from the apex. Chemiski et al. [20] defined new healthcare accelerators as pieces of equipment that included a dynamic wedge option (i.e., dynamic movement pairs of collimator jaws), which suits dose–rate modulation.

Improvement of dose uniformity for the actualization of target volume within the scope of radiation oncology led Saminathan et al. [21] to recommend the introduction of wedge filters and their dynamics to alter the structures of isodose curves. In a study of fluids with significant viscosity around two symmetric wedges, when the tangential velocity at the wedge's vertex is zero, Miksis and Vanden-Broeck [22] observed that fluids

of low viscosity contact back faster but fluids of high viscosity contact back at a longer time. The outcome of an analysis of bulk hydrodynamics on dynamics and statics wedge by Ruiz-Gutierrez et al. [23] revealed that the equilibrium contact angle of the fluid with the solid wedge and the opening angle of the wedge is needed for the characterization of confinement geometry and wetting properties of the fluid, respectively. The outcomes of a study on the importance of wedge angles within the interval $\pi/3 \le \beta\pi \le 5\pi/6$ and variation of acceleration rates $0 \le p \le 1$ suggest that fluid substance on the leeward side ends up closer to the spiral core. Moreover, the creation of the envelope that enfolds all other streaklines completely is possible due to fluid substances on the windward side of the wedge; see Xu [24]. Without losing generality, it is worth noting that there is either little information or no report on the dynamics of unsteady bioconvective ternary hybrid nanofluids on wedges focusing on a comparative analysis of the suspended three types of nanoparticles with small and moderately large thermal conductivity. The following are the main study areas that will aid in the discovery of transport phenomena:

1. What effect does rising stretching of wall velocity on the wedge have on the velocity of water conveying small and large thermal conductivity?
2. How does the wedge flow of ternary hybrid nanofluids carrying smaller and bigger thermal conductivity of nanoparticles affect heat transfer, friction at the wall, mass transfer, and the distribution rate of motile gyrotactic organisms?
3. What effect does increasing the Péclet number and lengthening the wall at the wedge have on the dispersion of motile microorganisms within the domain of ternary hybrid nanofluids transmitting smaller and bigger thermal conductivity of nanoparticles?

2. Research Methodology

We appraised a two-dimensional motion of a water-based ternary hybrid nanofluid made up of three types of nanoparticles with larger and smaller magnitudes of thermal conductivity on a fixed wedge and a wedge with a stretchable wall, as depicted in Figure 1. The $x-$axis and $y-$axis are the distances along the surface and perpendicular to the surface. The velocities are $v(t, x, y)$ and $u(t, x, y)$ in both directions. The changes in the potential flow velocity u_e with time and distance parallel to the wall greatly generate the transport phenomena in the dynamics of ternary hybrid nanofluids along the wedges. The pressure changes that induce the flow parallel to the $x-$axis for the unsteady flow of water-based ternary hybrid nanofluids on wedges are

$$-\frac{1}{\rho_{tf}}\frac{dp}{dx} = \frac{\partial u_e}{\partial t} + u_e \frac{\partial u_e}{\partial x} \tag{1}$$

where the external flow velocity far from the wall, wall velocity, and the Falkner–Skan power-law constant m are defined as

$$u_e(x,t) = \frac{ax^m}{1 - ct}, \quad u_w(x,t) = \frac{bx^m}{1 - ct}, \quad m = \frac{\beta}{2 - \beta} = \frac{\Omega}{2\pi - \Omega}, \quad \beta = \frac{\Omega}{\pi} = \frac{2m}{1 + m} \tag{2}$$
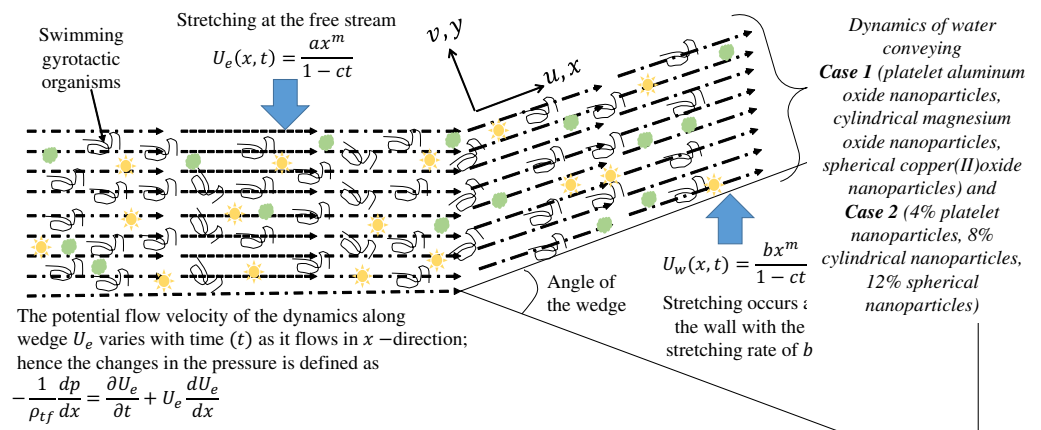
Figure 1. Physical configuration of the transport phenomena.

The ratio of the entire wedge angle $\Omega\pi$ is represented by the Hartree pressure gradient β. When $\Omega = 0$ implies $m = 0$, the dynamics on a converging channel are attainable for $\pi < \Omega < 2\pi$ and the well-known Blasius flow. In agreement with Raju et al. [25], Miksis and Vanden-Broeck [22], and Xu [24], the ideal set of equations to understand the comparative analysis is

$$\frac{tialu}{tialx} + \frac{tialv}{tialy} = 0,$$
(3)

$$\frac{\partial u}{\partial t} + v\frac{\partial u}{\partial y} + u\frac{\partial u}{\partial x} = u_e\frac{\partial u_e}{\partial x} + \frac{\partial u_e}{\partial t} + \frac{\mu_{tf}}{\rho_{tf}}\frac{\partial^2 u}{\partial y^2} + g\beta(T - T_\infty) + g\beta^*(C - C_\infty) + g\gamma(\rho_m - \rho_f)(N - N_\infty),$$
(4)

$$\frac{\partial T}{\partial t} + u\frac{\partial T}{\partial x} + v\frac{\partial T}{\partial y} = \frac{\kappa_{tf}}{(\rho c_p)_{tf}}\frac{\partial^2 T}{\partial y^2},$$
(5)

$$\frac{\partial C}{\partial t} + u\frac{\partial C}{\partial x} + v\frac{\partial C}{\partial y} = D_B\frac{\partial^2 C}{\partial y^2},$$
(6)

$$\frac{\partial N}{\partial t} + u\frac{\partial N}{\partial x} + v\frac{\partial N}{\partial y} + \frac{bw_c}{(C - C_\infty)}\frac{\partial}{\partial y}\left(N\frac{\partial C}{\partial y}\right) = D_m\frac{\partial^2 N}{\partial y^2}$$
(7)

For the static wedge, the wall velocity of the transport phenomenon is zero. The conditions worthy to be satisfied by the dynamics at the boundary are

$$u(t, x, 0) = 0, \quad v(t, x, 0) = 0, \quad T(t, x, 0) = T_w, \quad C(t, x, 0) = C_w, \quad N(t, x, 0) = N_w$$
(8)

$$u(t, x, \infty) \to u_e(t, x), \quad T(t, x, \infty) \to T_\infty, \quad C(t, x, \infty) \to C_\infty, \quad N(t, x, \infty) \to C_\infty.$$
(9)

For a moving wedge, the motion of the wedge is equivalent to the wall velocity $u_w(t, x)$. The boundary conditions for the dynamics are

$$u(t, x, 0) = u_w(t, x), \quad v(t, x, 0) = 0, \quad T(t, x, 0) = T_w, \quad C(t, x, 0) = C_w, \quad N(t, x, 0) = N_w$$
(10)

$$u(t, x, \infty) \to u_e(t, x), \quad T(t, x, \infty) \to T_\infty, \quad C(t, x, \infty) \to C_\infty, \quad N(t, x, \infty) \to C_\infty.$$
(11)

The dynamic viscosity, thermal conductivity, volume fraction, thermal volumetric expansion, density, and heat capacitance of the ternary hybrid nanofluid, defined by Wenhao Cao et al. [26], Song et al. [27], Timofeeva et al. [28], Elnaqeeb et al. [29], Ahammed et al. [30], Sahoo [31,32], Hamilton-Crosser [33], and Sahu and Sarkar [34], are defined as

$$\kappa_{hnf} = \frac{\kappa_{nf1}\phi_3 + \kappa_{nf2}\phi_2 + \kappa_{nf3}\phi_1}{\phi}, \quad \mu_{hnf} = \frac{\mu_{nf1}\phi_3 + \mu_{nf2}\phi_1 + \mu_{nf3}\phi_3}{\phi}, \quad \phi = \phi_3 + \phi_2 + \phi_1$$
(12)

$$\rho_{hnf} = (1 - \phi_3 - \phi_2 - \phi_1)\rho_{bf} + \phi_3\rho_{sp3} + \phi_2\rho_{sp2} + \phi_1\rho_{sp1}.$$
(13)

$$\beta_{hnf} = (1 - \phi_3 - \phi_2 - \phi_1)\beta_{bf} + \phi_3\beta_{sp3} + \phi_2\beta_{sp2} + \phi_1\beta_{sp1}. \tag{14}$$

$$(\rho c_p)_{hnf} = (1 - \phi_3 - \phi_2 - \phi_1)(\rho c_p)_{bf} + \phi_3(\rho c_p)_{sp3} + \phi_2(\rho c_p)_{sp2} + \phi_1(\rho c_p)_{sp1} \tag{15}$$

Table 1 presents the details of the adopted platelet, spherical, and cylinder tiny particles for viscosity and thermal conductivity models

$$\mu_{nf1} = (6.2\phi^2 + 2.5\phi + 1)\mu_{bf}, \quad \mu_{nf2} = (904.4\phi^2 + 13.5\phi + 1)\mu_{bf},$$

$$\mu_{nf3} = (612.6\phi^2 + 37.1\phi + 1)\mu_{bf}, \quad \kappa_{nf3} = \kappa_{bf}\left[\frac{-4.7\phi(\kappa_{bf} - k_{sp3}) + 4.7\kappa_{bf} + \kappa_{sp3}}{\phi(\kappa_{bf} - \kappa_{sp3}) + 4.7\kappa_{bf} + \kappa_{3sp3}}\right],$$

$$\kappa_{nf1} = \kappa_{bf}\left[\frac{-2\phi(\kappa_{bf} - \kappa_{sp1}) + 2\kappa_{bf} + \kappa_{sp1}}{\phi(\kappa_{bf} - \kappa_{sp1}) + 2\kappa_{bf} + \kappa_{sp1}}\right] \quad \kappa_{nf2} = \kappa_{bf}\left[\frac{-3.9\phi(\kappa_{bf} - \kappa_{sp2}) + 3.9\kappa_{bf} + \kappa_{sp2}}{\phi(\kappa_{bf} - \kappa_{sp2}) + 3.9\kappa_{bf} + \kappa_{2sp2}}\right] \tag{16}$$

At the wall of the static and dynamic wedge, the distribution of the gyrotactic microorganism Nm_x, quantifier for heat transfer Nu_x, quantifier for friction at the wall C_{fx}, and quantifier for mass transfer Sh_x are defined as

$$Nm_x = \frac{-x}{(N_w - N_\infty)}\frac{\partial N}{\partial y}\bigg|_{y=0}, \quad Nu_x = \frac{-x\kappa_{tf}}{\kappa_{bf}(T_w - T_\infty)}\frac{\partial T}{\partial y}\bigg|_{y=0} \quad C_{fx} = \frac{\mu_{tf}}{\rho_{bf}U_w^2(x)}\frac{\partial u}{\partial y}\bigg|_{y=0},$$

$$Sh_x = \frac{-x}{(C_w - C_\infty)}\frac{\partial C}{\partial y}\bigg|_{y=0}. \tag{17}$$

The transport phenomenon does not occur at several crucial points in fluid flow systems under complex flow conditions despite the emergence of bioconvection described above, and the velocity of the gyrotactic microorganisms is not distinct from the velocity of the ternary hybrid nanofluid. Furthermore, the transport phenomena under discussion do not involve the interaction flow of two or more separate phases with common interfaces. Due to the lack of several states or phases and various chemical properties, the single-phase model was taken into consideration in light of the aforementioned facts.

Table 1. Details of platelet magnesium oxide nanoparticles from Animasaun et al. [35], cylindrical aluminum oxide nanoparticles from Ref. [36], spherical silicon dioxide nanoparticles from Refs. [36,37], single-wall carbon nanoparticles by Kandasamy et al. [38], and water.

	ρ (kgm^{-3})	κ (W/mK)	c_p (J/kgK)	P_r
Water H$_2$O	997.1	0.613	4180	6.1723
Platelet SWCNT	2600	6600	425	
Cylindrical SWCNT	2600	6600	425	
Spherical SWCNT	2600	6600	425	
Platelet MgO	3580	48.4	960	
Cylindrical Al$_2$O$_3$	3970	40	765	
Spherical SiO$_2$	3970	36	765	

Similarity Variables

The following variables are used to transform and non-dimensionalize the dimensional governing equation

$$\frac{\eta}{y} = \sqrt{\frac{(m+1)u_o}{2\vartheta_{bf}x}}, \quad \theta(\eta) = \frac{T - T_\infty}{T_w - T_\infty}, \quad \frac{\psi(x,y)}{f(\eta)} = \sqrt{\frac{2\vartheta_{bf}xu_o}{m+1}}, \quad \aleph(\eta) = \frac{-C_\infty + C}{C_w - C_\infty}, \quad \lambda = \frac{b}{a}$$

$$\chi(\eta) = \frac{-N_\infty + N}{N_w - N_\infty}, \quad v = -\frac{\partial\psi}{\partial x}, \quad u = \frac{\partial\psi}{\partial y}, \quad P_r = \frac{\mu_{bf}Cp_{bf}}{\kappa_{bf}}, \quad S_c = \frac{\vartheta_{bf}}{D_B}, \quad S_{mm} = \frac{v_{bf}}{D_m},$$

$$Gt_{bf} = \frac{gx\beta(T_w - T_\infty)}{u_e^2}, \quad Gc_{bf} = \frac{gx\beta^*(C_w - C_\infty)}{u_e^2}, \quad R_b = \frac{gx\gamma(\rho_m - \rho_f)(N_w - N_\infty)}{u_e^2},$$

$$A = \frac{c}{x^{m-1}a}, \quad P_e = \frac{bW_c}{D_m}, \quad E_8 = \frac{-4.7\phi(\kappa_{bf} - k_{sp3}) + 4.7\kappa_{bf} + \kappa_{sp3}}{\phi(\kappa_{bf} - \kappa_{sp3}) + 4.7\kappa_{bf} + \kappa_{3sp3}}, \quad E_{10} = E_6\phi_1 + E_7\phi_2 + E_8\phi_3,$$

$$E_1 = 6.2\phi^2 + 2.5\phi + 1, \quad E_2 = 904.4\phi^2 + 13.5\phi + 1, \quad E_3 = 612.6\phi^2 + 37.1\phi + 1,$$

$$E_4 = E_1\phi_1 + E_2\phi_2 + E_3\phi_3, \quad E_5 = 1 - \phi_1 - \phi_2 - \phi_3 + \phi_1\frac{\rho_{sp1}}{\rho_{bf}} + \phi_2\frac{\rho_{sp2}}{\rho_{bf}} + \phi_3\frac{\rho_{sp3}}{\rho_{bf}},$$

$$E_6 = \frac{-2\phi(\kappa_{bf} - \kappa_{sp1}) + 2\kappa_{bf} + \kappa_{sp1}}{\phi(\kappa_{bf} - \kappa_{sp1}) + 2\kappa_{bf} + \kappa_{sp1}}, \quad E_7 = \frac{-3.9\phi(\kappa_{bf} - \kappa_{sp2}) + 3.9\kappa_{bf} + \kappa_{sp2}}{\phi(\kappa_{bf} - \kappa_{sp2}) + 3.9\kappa_{bf} + \kappa_{2sp2}},$$

$$E_9 = 1 - \phi_1 - \phi_2 - \phi_3 + \phi_1\frac{(\rho c_p)_{sp1}}{(\rho c_p)_{bf}} + \phi_2\frac{(\rho c_p)_{sp2}}{(\rho c_p)_{bf}} + \phi_3\frac{(\rho c_p)_{sp3}}{(\rho c_p)_{bf}}. \tag{18}$$

The dimensionless governing equations are

$$(m+1)\frac{E_4}{\phi E_5}\frac{d^3f}{d\eta^3} + 2A + 2m - A\eta\frac{d^2f}{d\eta^2} - 2A\frac{df}{d\eta} + f\frac{d^2f}{d\eta^2} + 2G_t\theta + 2\aleph G_c + 2R_b\chi = 0, \tag{19}$$

$$(m+1)\frac{E_{10}}{\phi E_9}\frac{d^2\theta}{d\eta^2} - P_r A\eta\frac{d\theta}{d\eta} + P_r f\frac{d\theta}{d\eta} = 0, \tag{20}$$

$$(m+1)\frac{d^2\aleph}{d\eta^2} - S_c A\eta\frac{d\aleph}{d\eta} + S_c f\frac{d\aleph}{d\eta} = 0, \tag{21}$$

$$(m+1)\frac{d^2\chi}{d\eta^2} - S_{mm}A\eta\frac{d\chi}{d\eta} + S_{mm}f\frac{d\chi}{d\eta} - P_e(m+1)\left(\chi\frac{d^2\aleph}{d\eta^2} + \frac{d\aleph}{d\eta}\frac{d\chi}{d\eta}\right) = 0. \tag{22}$$

For static wedge $\lambda = 0$, the fluid dynamics is bounded as

$$\theta = 1, \quad f = 0, \quad \frac{df}{d\eta} = \lambda, \quad \aleph = 1, \quad \chi = 1 \quad at \quad \eta = 0 \tag{23}$$

$$\theta \to 0, \quad \frac{df}{d\eta} \to 1, \quad \aleph \to 0, \quad \chi \to 0 \quad as \quad \eta \to \infty \tag{24}$$

For a moving wedge ($\lambda \neq 0$) at the wall ($\eta = 0$). As the boundary layer flow is induced, λ quantifies the movement of the wedge and the free stream flow. The dimensionless physical quantities are

$$\frac{Nm_x}{\sqrt{Re_x}}\sqrt{\frac{2}{m+1}} = -\chi'(0), \quad \frac{\phi Nu_x}{E_{10}\sqrt{Re_x}}\sqrt{\frac{2}{m+1}} = -\theta'(0), \quad \frac{\phi C_{fx}\sqrt{Re_x}}{E_4}\sqrt{\frac{2}{m+1}} = f''(0)$$

$$\frac{Sh_x}{\sqrt{Re_x}}\sqrt{\frac{2}{m+1}} = -\aleph'(0). \tag{25}$$

3. Numerical Integration and Validation

To obtain the numerical solution of Equations (19)–(24), the Runge–Kutta integration scheme (`rk4sh`) and collocation-s-hooting technique `bvp4c` package of MATLAB were employed. For the sake of conciseness, the descriptions of the numerical approaches given above by Kierzenka and Shampine [39], Al-Mdallal et al. [40], de Hoog and Weiss [41], and Animasaun [42] were rigorously adhered to. The dependent variables are $f(\eta)$, $f'(\eta)$, $f''(\eta)$, $\theta(\eta)$, $\theta'(\eta)$, $\aleph(\eta)$, $\aleph'(\eta)$, $\chi(\eta)$, $\chi'(\eta)$, $f''(0)$, $-\theta'(0)$, $-\aleph'(0)$, and $-\chi'(0)$. The nomenclature of the dependent variables listed in Section 3 that are needed in this study are diffusion of motile gyrotactic organisms away from the heated wall and across the ternary hybrid nanofluid, the distribution of motile gyrotactic organisms in the ternary hybrid

nanofluid, the mass movement via the hot wedge and the immediately surrounding layer, the concentration of the species that formed the ternary hybrid nanofluid, the shear stress function, the horizontal velocity function, the vertical velocity function, the temperature gradient function, the temperature distribution function, the concentration gradient function, the gradient of distribution of motile gyrotactic organisms, the heat transfer through the heated wedge and immediate adjacent layer, and the friction between the upper surface of the wedge and the last layer of the flowing fluid.

Results Validation

By juxtaposing the results of the same problem by utilizing the various approaches to the solution (`bvp4c` and `rksh`), the authors established the credibility of the integration technique. The limiting case for the dynamics on a wedge involved a colloidal mixture of water with platelet magnesium oxide nanoparticles, cylindrical aluminum oxide nanoparticles, and spherical titanium dioxide nanoparticles. The data used for the validation were $m = 0.1$, $G_t = G_c = R_b = 1$, $P_r = 6.1723$, $S_c = S_{mm} = 0.62$, $P_e = 0.5$, $\phi_1 = \phi_2 = \phi_3 = 0.1$, $\rho_{bf} = 997.1$, $\kappa_{bf} = 0.613$, and $Cp_{bf} = 4,180$ when (i.e., $A = 0.1, 0.2, 0.3$). Tables 2 and 3 indicate that the numerical approach for both numerical methods is valid and that the findings are dependable to an acceptable degree for investigating transport phenomena.

Table 2. Reliance on numerical integration for static wedge $\lambda = 0$ and $\eta_\infty = 5$.

A	rk4sh $f''(0)$	bvp4c $f''(0)$	rk4sh $-\theta'(0)$	bvp4c $-\theta'(0)$
0.1	0.451206374602597	0.451206301040792	0.453340211815564	0.453340295041978
0.2	0.475722148811551	0.475722187415029	0.371908418391181	0.371908400147596
0.3	0.502553781403640	0.502553744719328	0.289615627410633	0.289615696031472

Table 3. Reliance on numerical integration for moving wedge $\lambda = 1$ and $\eta_\infty = 5$.

A	rk4sh $f''(0)$	bvp4c $f''(0)$	rk4sh $-\theta'(0)$	bvp4c $-\theta'(0)$
0.1	0.149083116414503	0.149083185741905	1.060073047726859	1.060073096024179
0.2	0.154286959072002	0.154286985741906	1.003808597826008	1.0038085997400126
0.3	0.160265225109621	0.160265254127903	0.944589109510400	0.9445891784519038

4. Analysis of Results and Discourse

This section presents an examination and discourse of the findings from the governing equation that describes cases 1 and 2 of the transport phenomena. This section discusses the first case and the dynamics of water composed of SWNCT nanoparticles with thermal conductivity of a larger magnitude. The second scenario is detailed, which is the transport phenomena composed of water conveying smaller magnitudes of thermal conductivity (i.e., platelet magnesium oxide, cylindrical aluminum oxide, and spherical silicon dioxide nanoparticles). It is worth noting that the nanoparticles created in scenario 2 of the transport phenomena are incredibly dense; see Table 1.

4.1. Analysis of Results

When $A = 0.5$, $m = 0.1$, $G_t = G_c = R_b = 1$, $P_r = 6.1723$, $S_c = S_{mm} = 0.62$, $P_e = 0.5$, $\phi_1 = \phi_2 = \phi_3 = 0.1$, $\rho_{bf} = 997.1$, $\kappa_{bf} = 0.613$, and $Cp_{bf} = 4,180$, the parameter that quantifies the stretching velocity at the wall of the wedge increases within the interval $0 \leq \lambda \leq 2$. It can be seen in Figures 2 and 3 that the velocities for the two transport phenomena increase due to a higher stretching rate b of the wall velocity $u_w(x,t)$. The differences between the two transport phenomena for the two cases are only significant when the wedge is stagnant and moves slowly (i.e., $0 \leq \lambda \leq 0.5$). As shown in Figure 4,

the temperature distribution across the transport phenomenon declines with higher levels of stretching wall velocity (λ). This study observed optimal shear stress proportional to friction within the domain $0 \leq \eta \leq 5$. Moreover, higher temperature distributions across both ternary hybrid nanofluids and the maximum species (i.e., concentration) of the ternary hybrid nanofluids are not far-fetched. A wider distribution of motile gyrotactic organisms within the domain $0 \leq \eta \leq 5$ was found when the wedge was static (i.e., $\lambda = 0$). These results are not presented for brevity but are worthy to be mentioned. In the case of the static wedge (i.e., $\lambda = 0$), there exists an optimal significant difference in the velocity, temperature distribution, concentration, and distribution of motile gyrotactic organisms across the domain between case 1 and case 2.
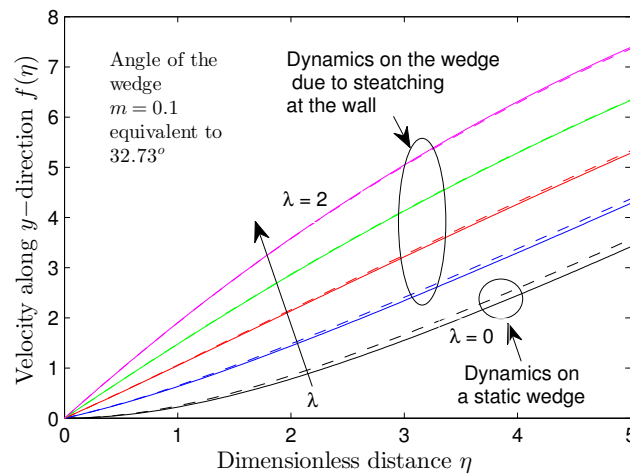

Figure 2. Effect of wall stretching velocity λ on the velocity of both fluids along the $y-$direction when $m = 0.1$
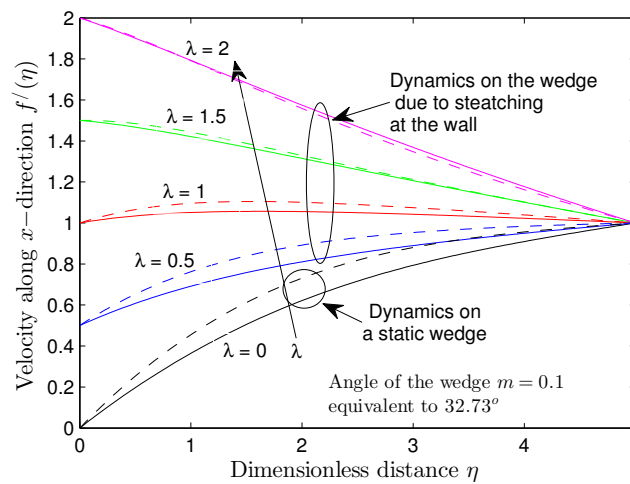

Figure 3. Effect of wall stretching velocity λ on the dynamics of both ternary hybrid nanofluids along $x-$direction when $m = 0.1$
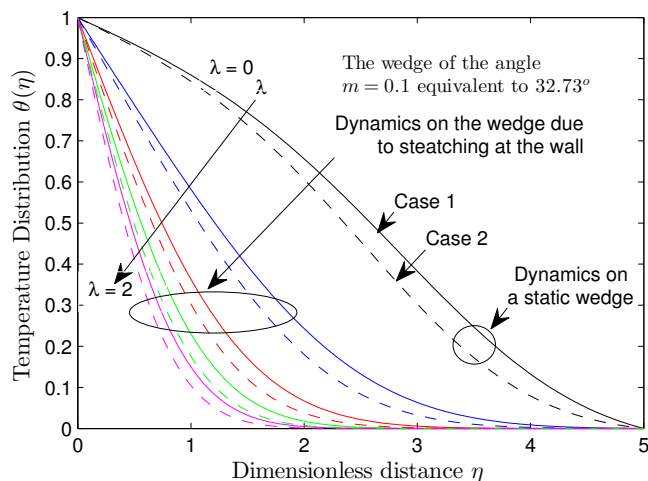
Figure 4. Effect of wall stretching velocity λ on the temperature distribution within the dynamics of both nanofluids when $m = 0.1$.

After generating the appropriate data using the integration technique mentioned above, data were moved to Surfer Version 11.1.719. The Kriging method of data gridding was used to generate the contour results presented in this section. Figures 5 and 6 show that $f''(\eta)$ declines as λ rises. Tables 4 and 5 show that the friction at the wall reduces due to a higher level of wall stretching velocity. These figures present the variations in the function that represents the shear stress at different levels of wall stretching on the wedge (λ) for the transport phenomena of cases 1 and 2. It is evident that the most minimum shear stresses, denoted as $\frac{\phi C_{fx}\sqrt{Re_x}}{E_4}\sqrt{\frac{2}{m+1}}$, occur at larger values of λ near the wall. At $\eta = 0$, $f''(\eta)$ decreases significantly with λ. At the other end, $\eta = 0$, $f''(\eta)$ decreases moderately with λ. In case 1 transport phenomenon presented as Table 4, $\frac{\phi C_{fx}\sqrt{Re_x}}{E_4}\sqrt{\frac{2}{m+1}}$ decreases with λ at the rate of -0.329789963. However, for the case 2 transport phenomenon, $\frac{\phi C_{fx}\sqrt{Re_x}}{E_4}\sqrt{\frac{2}{m+1}}$ decreases with λ at the rate of -0.356473325; see Table 5. As shown in Figures 7–10, the transfer of heat energy and transfer of species that form the nanofluids increase significantly with λ near the wall. In other words, increasing wall stretching on the wedge leads to a higher heat transfer commensurate with the Nusselt number and broader mass transfer commensurate with the Sherwood number in Equation (25).

Table 4. Variation of physical quantities for case 1—larger thermal conductivity of nanoparticles when $\eta_\infty = 5$.

λ	$\frac{\phi C_{fx}\sqrt{Re_x}}{E_4}\sqrt{\frac{2}{m+1}}$	$\frac{\phi Nu_x}{E_{10}\sqrt{Re_x}}\sqrt{\frac{2}{m+1}}$	$\frac{Sh_x}{\sqrt{Re_x}}\sqrt{\frac{2}{m+1}}$	$\frac{Nm_x}{\sqrt{Re_x}}\sqrt{\frac{2}{m+1}}$
0	0.501391652	0.126832395	0.164413180	0.198769191
0.5	0.313117110	0.425081500	0.322440050	0.449063565
1.0	0.145577661	0.721081217	0.492851011	0.704626364
1.5	−0.009437541	0.961784227	0.644943911	0.926617648
2.0	−0.161805929	1.163072510	0.776441110	1.116848885
S_{lp}	−0.329789963	0.521836591	0.309311944	0.462742694

$A = 0.5$, $m = 0.1$, $G_t = G_c = R_b = 1$, $P_r = 6.1723$, $S_c = S_{mm} = 0.62$, $P_e = 0.5$, $\phi_1 = \phi_2 = \phi_3 = 0.1$, $\rho_{bf} = 997.1$, $\kappa_{bf} = 0.613$, and $Cp_{bf} = 4180$.

Table 5. Variation of physical quantities for case 2—smaller thermal conductivity of nanoparticles when $\eta_\infty = 5$.

λ	$\dfrac{\phi C_{fx}\sqrt{Re_x}}{E_4}\sqrt{\dfrac{2}{m+1}}$	$\dfrac{\phi Nu_x}{E_{10}\sqrt{Re_x}}\sqrt{\dfrac{2}{m+1}}$	$\dfrac{Sh_x}{\sqrt{Re_x}}\sqrt{\dfrac{2}{m+1}}$	$\dfrac{Nm_x}{\sqrt{Re_x}}\sqrt{\dfrac{2}{m+1}}$
0	0.562250645	0.137735549	0.179214207	0.221766375
0.5	0.356021584	0.480527624	0.331789925	0.462646012
1.0	0.17532672	0.815315534	0.497225412	0.710701282
1.5	0.008681269	1.086212765	0.646341186	0.928566151
2.0	−0.15526251	1.312552075	0.77611485	1.116477
S_{lp}	−0.356473325	0.591063639	0.301670509	0.451068278

$A = 0.5$, $m = 0.1$, $G_t = G_c = R_b = 1$, $P_r = 6.1723$, $S_c = S_{mm} = 0.62$, $P_e = 0.5$, $\phi_1 = \phi_2 = \phi_3 = 0.1$, $\rho_{bf} = 997.1$, $\kappa_{bf} = 0.613$, and $Cp_{bf} = 4180$.
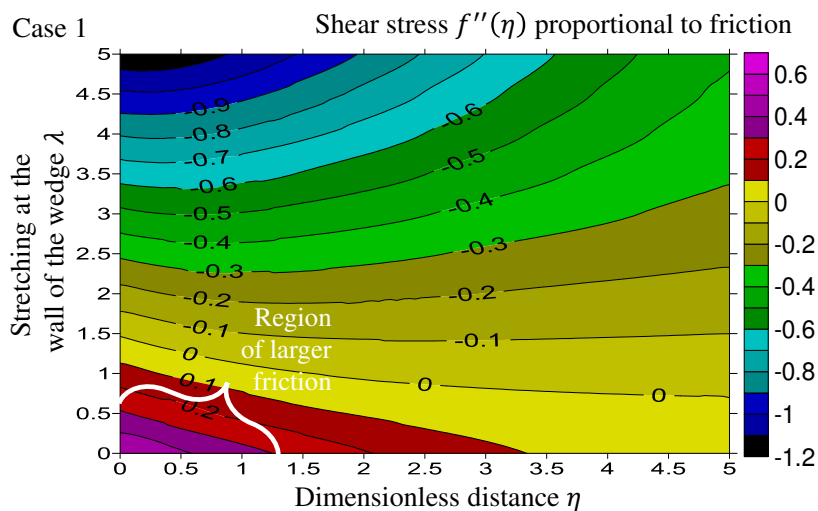
Figure 5. Changes in the shear stress function $f''(\eta)$ with the wall stretching velocity λ—case 1.
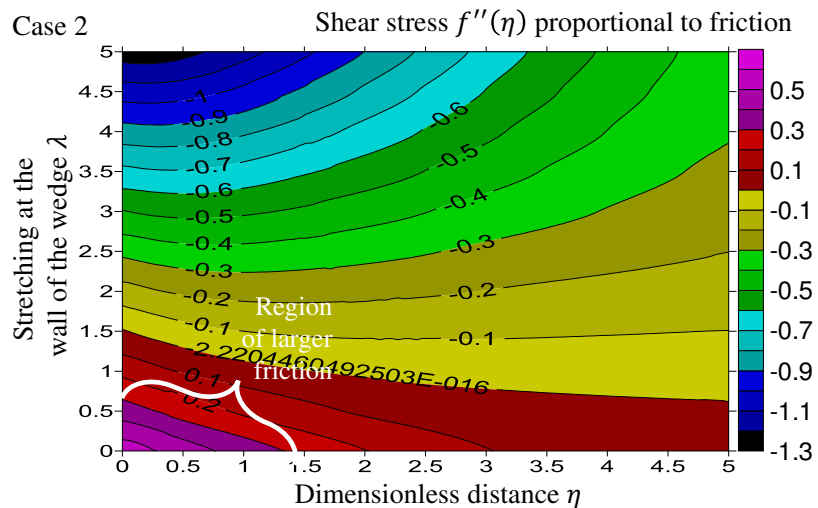

Figure 6. Changes in the shear stress function $f''(\eta)$ with the wall stretching velocity λ—case 2.
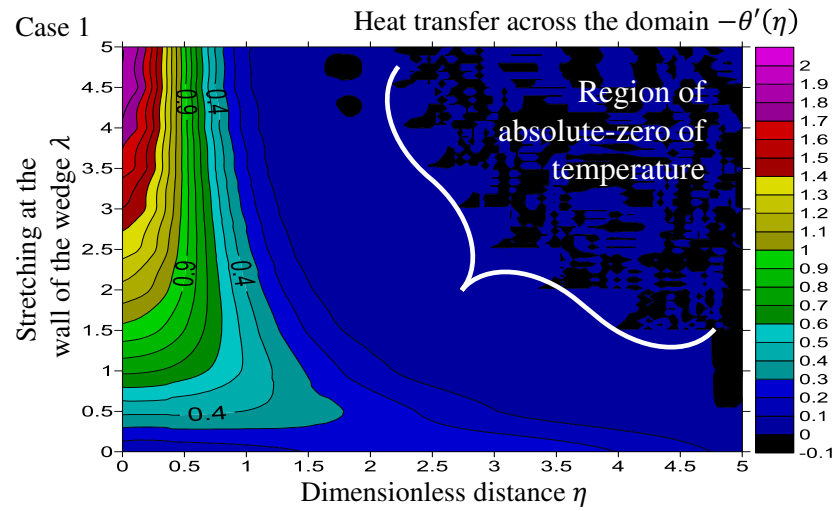
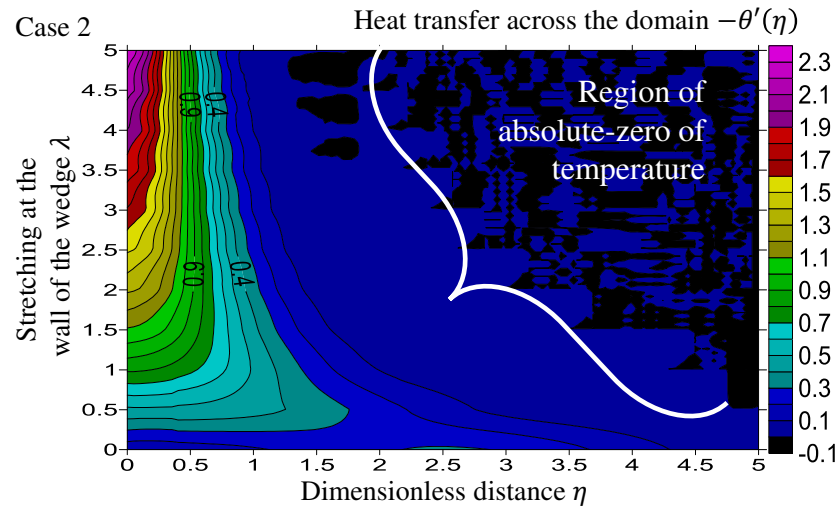**Figure 7.** Variation of the heat transfer $-\theta'(\eta)$ with the wall stretching velocity λ—case 1.

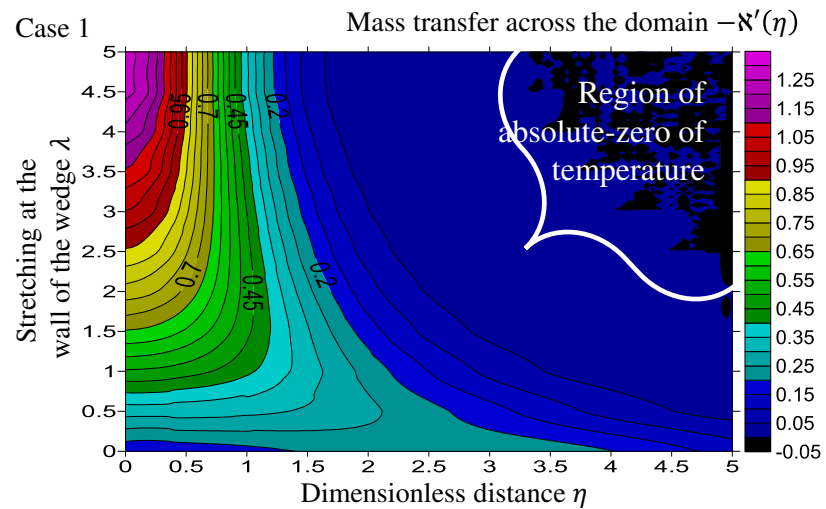**Figure 8.** Variation of the heat transfer $-\theta'(\eta)$ with the wall stretching velocity λ—case 2.

Figure 9. Variation of the mass transfer $-\aleph'(\eta)$ with the wall stretching velocity λ.
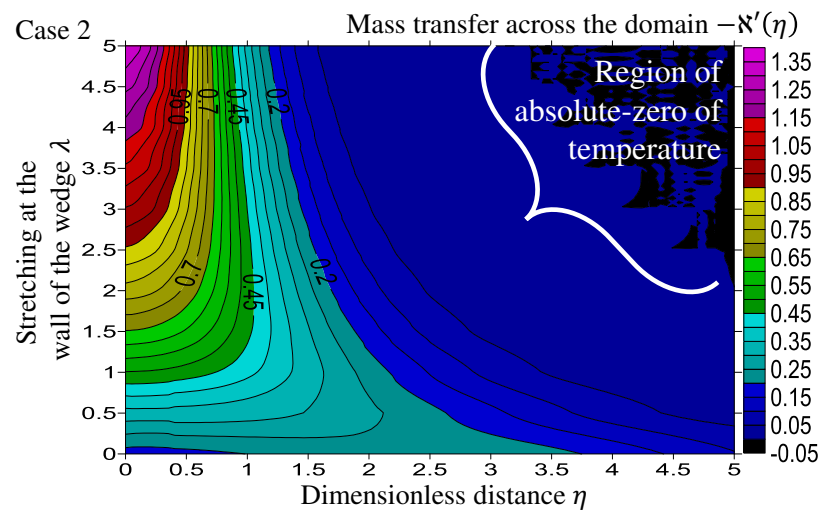
Figure 10. Variation of the gradient of distribution of motile gyrotactic organisms in the entire domain $-\chi'(\eta)$ with the wall stretching velocity λ.

The heat transfer across the case 1 transport phenomenon increases with λ at the rate of 0.521836591. Meanwhile, the heat transfer across the case 2 transport phenomenon increases with λ at the higher rate of 0.591063639; see Tables 4 and 5. The differences between the observed changes in the increase in mass transfer rate for the transport phenomena of cases 1 and 2 are minimal (regarding magnitude). Moreover, the distribution rate of motile gyrotactic organisms was found to be higher as $\lambda \to 2$ in Tables 4 and 5. Figures 11 and 12 depict the gradients of distribution of motile gyrotactic organisms across the domain at different levels of wall stretching velocity λ. Considering the first case of transport phenomenon, the effects of P_e on $-\chi'(\eta)$ when $\lambda = 0$ and $\lambda = 5$ were examined and presented as in Figures 13 and 14. The distribution of motile gyrotactic organisms $\chi(\eta)$ is a decreasing property of P_e. For the static wedge and moving wedge, the higher the Péclet number, the lower the distribution of motile microorganisms within the fluid domain Figures 13 and 14. Moreover, minimal distribution of motile microorganisms within the domain of the ternary hybrid nanofluid is obtainable when the wedge moves faster. Figures 15 and 16 confirm the rise of a gradient of distribution of motile gyrotactic organisms near the wall but reduced far away from the wedge as shown in the 3D plot.
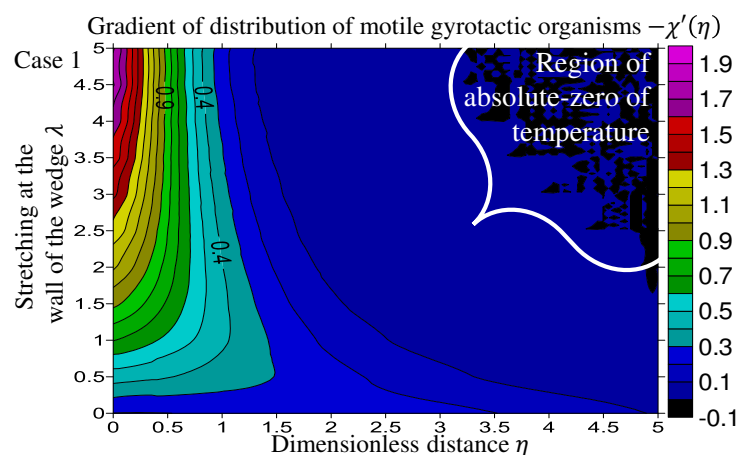

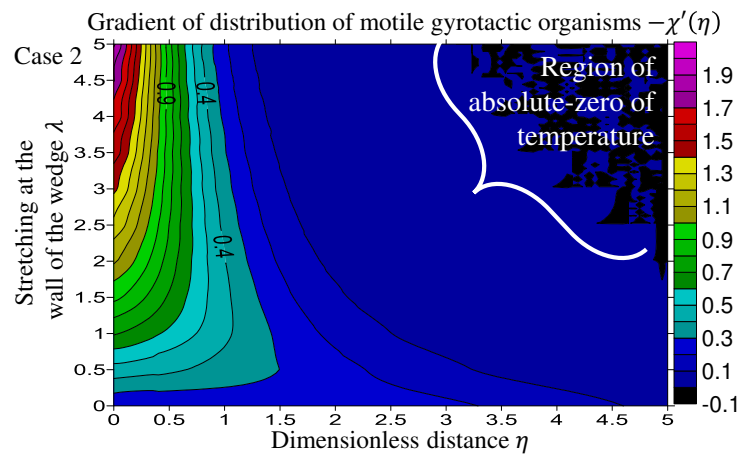**Figure 11.** Distribution of motile gyrotactic organisms within the entire domain $\chi(\eta)$ with λ when $\lambda = 0$—case 1.

Figure 12. Distribution of motile gyrotactic organisms within the entire domain $\chi(\eta)$ with λ when $\lambda = 0$—case 2.
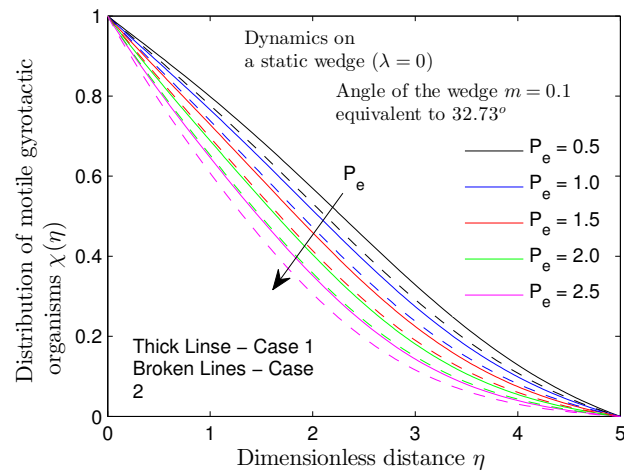

Figure 13. Distribution of motile gyrotactic organisms $\chi(\eta)$ within the entire domain on a static wedge with P_e when $\lambda = 0$.
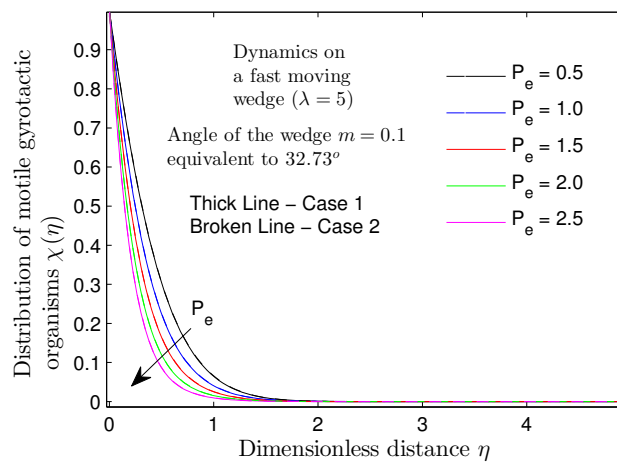

Figure 14. Distribution of motile gyrotactic organisms $\chi(\eta)$ within the entire domain on a fast-moving wedge with P_e when $\lambda = 5$.
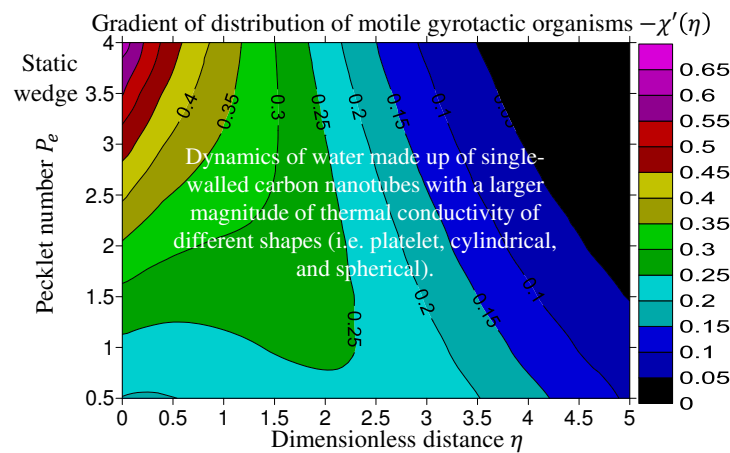
Figure 15. Variation of the gradient of distribution of motile gyrotactic organisms $-\chi'(\eta)$ within the entire domain on a static wedge (i.e., $\lambda = 0$) with P_e and $m = 0.1$.
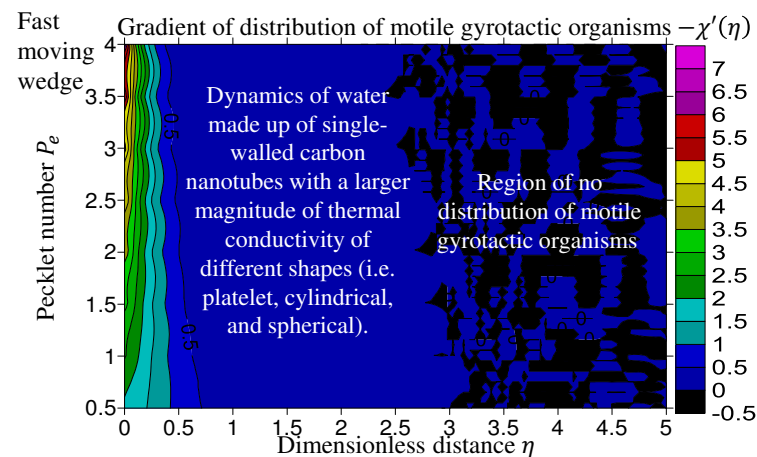

Figure 16. Variation of the gradient of distribution of motile gyrotactic organisms $-\chi'(\eta)$ within the entire domain on a fast-moving wedge (i.e., $\lambda = 5$) with P_e and $m = 0.1$.

The turning points are within the interval $0.5 \leq \eta \leq 2$. The distribution of motile microorganisms is extensive in Figure 15. It was also noticed that the maximum value of $-\chi'(\eta)$ was obtained when $P_e = 4$ at $\eta = 0$ as 6.8992. In Figure 15, when $\lambda = 0$ for a static wedge and $P_e = 0.5$, $\frac{Nm_x}{\sqrt{Re_x}}\sqrt{\frac{2}{m+1}}$ that quantifies the gradient of distribution of motile gyrotactic organisms at the wall decreases with η at the rate -0.020498425. When there exists a higher stretching at the wall of the wedge (i.e., $\lambda = 5$ and $P_e = 0.5$), $-\chi'(\eta)$ decreases with η at the rate of -0.130199045.

4.2. Discussion of the Results

Physically, as the wall velocity $u_w(x,t)$ increases, the layers of the ternary hybrid fluid on the wedge move in the same direction that boosts $v(t,x,y)$ and $u(t,x,y)$. The increment of stretching velocity at the wall of the wedge within the interval $0 \leq \lambda \leq 2$ implies that the wedge moves at an increasing rate with its pointed edge at the front. Higher λ was found capable of enhancing the velocity due to the viscous nature of the ternary hybrid nanofluid that declines when stretching rate b grows; see Figures 2 and 3. The observed increase in the velocity of both water-based ternary hybrid nanofluids parallel and perpendicular to the wedge surface is due to a higher stretching rate b of wall velocity $u_w(x,t)$, which is capable of reducing the viscosity; see Figures 2 and 3. The reduced viscosity of both fluids is used in the industry to facilitate the dynamics between two locations as temperature rises. The outcomes of the result in Figures 2–4 suggest that there exists a significant

difference between the velocities of case 1 and case 2 when the wedge is static. A higher level of wall stretching on the wedge (λ) generates greater pressure on the fluid flow; hence the changes in the shear stress are more significant at the wall compared to at the free stream; see Figures 5 and 6. A higher level of friction manifests when the wedge is static ($\lambda = 0$) as shown in Tables 4 and 5. It is worth noting that a higher local skin friction coefficient of 0.562250645 occurs in the case 2 transport phenomenon; see Table 5. When the wedge is static, the shear stress of the domain decreases across the domain at the rate of -0.329789963. However, when there is faster stretching at the wedge (λ), the shear stress across the domain increases at -0.356473325.

When the ternary hybrid nanofluid flows faster, a more significant amount of the substance is bound to move over the wedge surface within a short period. Thus, the average kinetic energy of nanoparticles and molecules forming the ternary hybrid nanofluid decreases. On the distribution of heat energy through the various layers of the atmosphere at different latitudes, McEwen [43] remarked that the temperature typically drops due to the surface's height. There is a possibility for decreasing temperature distribution as $\lambda \to 2$ because of the manifestation of the reduction of total surface energy; see Figure 4. According to Ruiz-Gutierrez (2018), there is an attempt to reduce a liquid droplet's total surface energy when it comes into contact with the inside walls of a channel that fits wedge-shaped. The primary source of energy dissipation near the wedge's apex is friction associated with a viscous force on the fluid flow, which balances the work rate conducted by capillary forces. Just because the higher distribution of temperature across the ternary hybrid nanofluid emerges when ($\lambda = 0$), the concentration and distribution of motile gyrotactic organisms were found to emerge when the wedge was static; see Figure 4. Consequently, stretching on the wedge can reduce the distribution of heat energy, concentration, and distribution of motile gyrotactic organisms across the domain; see Figures 7–12. Wall stretching boosts the pressure inducing the dynamics of each ternary hybrid nanofluid and the flow rate.

An increment in temperature distribution ought to manifest due to a rise in pressure. However, in this case, a larger volume of ternary hybrid nanofluid passes through the wedge surface at each unit of time. The mass transfer, heat transfer, and distribution of motile gyrotactic organisms across the domain become minimal when the nanoparticles' thermal conductivity is considerably large, as in the first case (i.e., water conveying platelet SWCNTs, cylindrical SWCNTs, and spherical SWCNTs). Carbon nanotubes carry heat through the vibrating of the covalent bonds keeping the carbon atoms connected. The carbon nanotubes atoms wig around and convey the heat through the base fluid, unlike metals, which rely on the flow of electrons. Single-walled carbon nanotubes show great promise for enhancing the thermal conductivity of traditional polymers. From Figures 7 and 8, one can see that the transfer of heat energy and mass transfer is predominant at a higher level of wall stretching on the wedge (λ). The net transfer of the species between two locations is referred to as mass transfer. Figures 9 and 10 reveal that the transfer of the species near the wall may be characterized as the mass in transit due to the gradient species concentration in the mixture. The distribution of motile gyrotactic organisms decreases with λ and also from the wall $\eta = 0$ to the free stream $\eta \to 5$, not because the distribution is maximal at the wall of the wedge and minimal at the free stream; Figures 11 and 12.

Flint and Burstein [44] identified the Péclet number as a valuable tool for assessing mixing since it is affected by stochastic particle drift caused by diffusion (i.e., mixing). The observed decrement in the concentration of motile microorganisms within the ternary hybrid fluid due to the rising Péclet number is traced to the associated maximization of temperature distribution across the domain. This is true because when the thermal conductivity of the three kinds of nanoparticles is large in magnitude, the ternary hybrid nanofluid conveys SWCNT nanoparticles, and the distribution of temperature increases with the rising Péclet number. However, this is higher than that of case 2, where the thermal conductivity of the nanoparticles is moderately small (i.e., platelet magnesium oxide nanoparticles, cylindrical aluminum oxide nanoparticles, spherical silicon dioxide nanoparticles); see Figures 13 and 14. Dey and Chutia [45] once noticed that the bioconvection raises the

microbe concentration across the flow zone. The collection of microorganisms is higher near the surface and eventually decreases as the perpendicular distance to the wall grows. With higher levels of the Schmidt number associated with bioconvection, the local density number of microorganisms decreases. Figures 15 and 16 reveal the gradient of distribution of motile gyrotactic organisms in a colloidal mixture of water and single-walled carbon nanotubes with a larger magnitude of thermal conductivity of different shapes (i.e., platelet, cylindrical, and spherical) when the wedge is static and moving faster (i.e., $\lambda = 5$). Similar to a moving conveyor belt, more tension is bound to manifest on the carrying side when the layers on the wedge move (i.e., $\lambda = 5$). Consequently, the distribution of motile gyrotactic organisms presented in Figure 16 only occurs near the wall. The observed optimal value of $-\chi'(\eta)$ that was obtained at $\eta = 0$ as 6.8992 can be traced to the heated wall and distribution of motile gyrotactic organisms that spread out quickly due to diffusive processes (i.e., $P_e = 4$).

5. Summary/Conclusions

We studied the dynamics of the unsteady motion of ternary hybrid nanofluid on static and moving wedges. The dynamics of water made up of (i) single-walled carbon nanotubes with a larger magnitude of thermal conductivity of different shapes (i.e., platelet, cylindrical, and spherical) and (ii) moderately small magnitude of thermal conductivity (i.e., platelet magnesium oxide, cylindrical aluminum oxide, spherical silicon dioxide). The following conclusions were drawn based on the findings of the analysis and discussion:

1. Increasing the stretching at the wedge's wall in the same direction as the transport phenomenon is suitable for decreasing the temperature distribution due to the higher velocity of ternary hybrid nanofluids either parallel or perpendicular to the wedge.
2. When the wedge is stationary or travels extremely slowly close to the wall, more friction is achievable at the wall. Although the second scenario of transport phenomena results in the highest friction coefficients along the wall, it is essential to note that increased wall stretching and the dispersion of SWCNTs in water make it possible to achieve the best increase in the same dependent variable.
3. Enhancement of stretching at the wedge wall is a factor responsible for causing a significant transfer of heat energy, species of the nanoparticles, and motile gyrotactic organisms near the wall only.
4. Significant difference exists between (a) the heat transfer of heat energy, (b) the mass transfer of species, and (c) the distribution rate of motile gyrotactic organisms in the dynamics of water made up of (i) single-walled carbon nanotubes with larger magnitudes of thermal conductivity of different shapes (i.e., platelet, cylindrical, and spherical) and (ii) a moderately small magnitude of thermal conductivity (i.e., platelet magnesium oxide, cylindrical aluminum oxide, spherical silicon dioxide).
5. When there is a more significant magnitude of thermal conductivity but smaller densities, and heat capacity of the three types of nanoparticles, as in the case of SWCNTs, the diffusion of motile gyrotactic organisms is significantly influenced in the motion of the bioconvective ternary hybrid nanofluid on a static wedge.

Further study of the dynamics through cavities with or without fins is necessary to grasp the motion outside the boundary layer.

Author Contributions: Conceptualization, I.L.A., Q.M.A.-M. and U.K.; methodology, I.L.A., Q.M.A.-M., U.K. and A.S.A.; software, Q.M.A.-M., U.K.; validation, I.L.A., Q.M.A.-M. and U.K.; formal analysis, I.L.A., Q.M.A.-M. and U.K.; investigation, Q.M.A.-M., U.K.; resources, I.L.A.; data curation, I.L.A., U.K.; writing—original draft preparation, I.L.A., Q.M.A.-M. and U.K.; writing—review and editing, I.L.A., Q.M.A.-M., U.K. and A.S.A.; visualization, Q.M.A.-M.; supervision, Q.M.A.-M. and A.S.A.; project administration, Q.M.A.-M. and A.S.A. All authors have read and agreed to the published version of the manuscript.

Conflicts of Interest: On behalf of all authors, the corresponding author states that there is no conflict of interest.

References

1. Baughman, R.H.; Zakhidov, A.A.; De Heer, W.A. Carbon nanotubes—The route toward applications. *Science* **2002**, *297*, 787–792. [CrossRef] [PubMed]
2. Kim, P.; Shi, L.; Majumdar, A.; McEuen, P.L. Thermal transport measurements of individual multiwalled nanotubes. *Phys. Rev. Lett.* **2001**, *87*, 215502. [CrossRef] [PubMed]
3. Prasek, J.; Drbohlavova, J.; Chomoucka, J.; Hubalek, J.; Jasek, O.; Adam, V.; Kizek, R. Methods for carbon nanotubes synthesis. *J. Mater. Chem.* **2011**, *21*, 15872–15884. [CrossRef]
4. Dai, H. Carbon nanotubes: Synthesis, integration, and properties. *Accounts Chem. Res.* **2002**, *35*, 1035–1044. [CrossRef]
5. Li, H.; He, X.; Liu, Y.; Yu, H.; Kang, Z.; Lee, S.T. Synthesis of fluorescent carbon nanoparticles directly from active carbon via a one-step ultrasonic treatment. *Mater. Res. Bull.* **2011**, *46*, 147–151. [CrossRef]
6. Zhang, B.; Liu, C.Y.; Liu, Y. A novel one-step approach to synthesize fluorescent carbon nanoparticles. *Eur. J. Inorg. Chem.* **2010**, *2010*, 4411–4414. [CrossRef]
7. Li, Y.-H.; Qu, W.; Feng, J.-C. Temperature dependence of thermal conductivity of nanofluids. *Chin. Phys. Lett.* **2008**, *25*, 3319. [CrossRef]
8. Maranville, C.; Bollin, S.C.; Sawall, D.; Ohtani, H.; Remillard, J.T.; Ginder, J.M. Thermal conductivity of single-wall carbon nanotube dispersions: Role of interfacial effects. *J. Phys. Chem. C* **2008**, *112*, 654–658. [CrossRef]
9. Sabiha, M.A.; Mostafizur, R.M.; Saidur, R.; Mekhilef, S. Experimental investigation on thermo physical properties of single walled carbon nanotube nanofluids. *Int. J. Heat Mass Transf.* **2016**, *93*, 862–871. [CrossRef]
10. Said, Z. Thermophysical and optical properties of SWCNTs nanofluids. *Int. Commun. Heat Mass Transf.* **2016**, *78*, 207–213. [CrossRef]
11. Namarvari, H.; Razmara, N.; Meneghini, J.R.; Mir, C.R. Effect of SWCNT volume fraction on the viscosity of water-based nanofluids. *J. Mol. Model.* **2021**, *27*, 253. [CrossRef] [PubMed]
12. Alqahtani, A.M.; Adnan, Khan, U.; Ahmed, N.; Mohyud-Din, S.T.; Khan, I. Numerical investigation of heat and mass transport in the flow over a magnetized wedge by incorporating the effects of cross-diffusion gradients: Applications in multiple engineering systems. *Math. Probl. Eng.* **2020**, *2020*, 1–10. [CrossRef]
13. Sarkar, S.; Endalew, M.F. Effects of melting process on the hydromagnetic wedge flow of a Casson nanofluid in a porous medium. *Bound. Value Probl.* **2019**, *2019*, 43. [CrossRef]
14. Jameson, A. Iterative solution of transonic flows over airfoils and wings, including flows at Mach 1. *Commun. Pure Appl. Math.* **1974**, *27*, 283–309. [CrossRef]
15. Stewartson, K. Further solutions of the Falkner-Skan equation. *Math. Proc. Camb. Philos. Soc.* **1954**, *50*, 454–465. [CrossRef]
16. Riccardi, G.; Iafrati, A. Water impact of an asymmetric floating wedge. *J. Eng. Math.* **2004**, *49*, 19–39. [CrossRef]
17. Makinde, O.D.; Animasaun, I.L. Bioconvection in MHD nanofluid flow with nonlinear thermal radiation and quartic autocatalysis chemical reaction past an upper surface of a paraboloid of revolution. *Int. J. Therm. Sci.* **2016**, *109*, 159–171. [CrossRef]
18. Makinde, O.D.; Animasaun, I.L. Thermophoresis and Brownian motion effects on MHD bioconvection of nanofluid with nonlinear thermal radiation and quartic chemical reaction past an upper horizontal surface of a paraboloid of revolution. *J. Mol. Liq.* **2016**, *221*, 733–743. [CrossRef]
19. Schlichting, H. *Boundary-Layer Theory*; McGraw-Hill: New York, NY, USA, 1968.
20. Chelminski, K.; Bulski, W.; Rostkowska, J.; Kania, M. Dynamic wedges-dosimetry and quality control. *Rep. Pract. Oncol. Radiother.* **2006**, *11*, 67–75. [CrossRef]
21. Saminathan, S.; Manickam, R.; Supe, S.S. Comparison of dosimetric characteristics of physical and enhanced dynamic wedges. *Rep. Pract. Oncol. Radiother.* **2012**, *17*, 4–12. [CrossRef]
22. Miksis, M.J.; Vanden-Broeck, J.M. Self-similar dynamics of a viscous wedge of fluid. *Phys. Fluids* **1999**, *11*, 3227–3231. [CrossRef]
23. Ruiz-Gutierrez, E.; Semprebon, C.; McHale, G.; Ledesma-Aguilar, R. Statics and dynamics of liquid barrels in wedge geometries. *J. Fluid Mech.* **2018**, *842*, 26–57. [CrossRef]
24. Xu, L. Accelerating viscous flow past a wedge. *Phys. Fluids* **2020**, *32*, 013604. [CrossRef]
25. Raju, C.S.K.; Hoque, M.M.; Sivasankar, T. Radiative flow of Casson fluid over a moving wedge filled with gyrotactic microorganisms. *Adv. Powder Technol.* **2017**, *28*, 575–583. [CrossRef]
26. Cao, W.; Animasaun, I.L.; Yook, S.-J.; Oladipupo, V.A.; Ji, X. Simulation of the dynamics of colloidal mixture of water with various nanoparticles at different levels of partial slip: Ternary-hybrid nanofluid. *Int. Commun. Heat Mass Transf.* **2022**, *135*, 106069. [CrossRef]

27. Song, Y.-Q.; Obideyi, B.D.; Animasaun, I.L.; Mahrous, Y.M.; Chung, J.D. Significance of haphazard motion and thermal migration of alumina and copper nanoparticles across the dynamics of water and ethylene glycol on a convectively heated surface. *Case Stud. Therm. Eng.* **2021**, *26*, 101050. [CrossRef]

28. Timofeeva, E.V.; Routbort, J.L.; Singh, D. Particle shape effects on thermophysical properties of alumina nanofluids. *J. Appl. Phys.* **2009**, *106*, 014304. [CrossRef]

29. Elnaqeeb, T.; Animasaun, I.L.; Shah, N.A. Ternary-hybrid nanofluids: Significance of suction and dual-stretching on three-dimensional flow of water conveying nanoparticles with various shapes and densities. *Z. Fur Naturforschung A* **2021**, *76*, 231–243. [CrossRef]

30. Ahammed, N.; Asirvatham, L.G.; Wongwises, S. Entropy generation analysis of graphene-alumina hybrid nanofluid in multiport minchannel heat exchanger coupled with thermoelectric cooler. *Int. J. Heat Mass Transf.* **2016**, *103*, 1084–1097. [CrossRef]

31. Sahoo, R.R. Heat transfer and second law characteristics of radiator with dissimilar shape nanoparticle-based ternary hybrid nanofluid. *J. Therm. Anal. Calorim.* **2020**, *146*, 827–839. [CrossRef]

32. Sahoo, R.R. Thermo-hydraulic characteristics of radiator with various shape nanoparticle-based ternary hybrid nanofluid. *Powder Technol.* **2020**, *370*, 19–28. [CrossRef]

33. Hamilton, R.L.; Crosser, O.K. Thermal Conductivity of Heterogeneous Two-Component Systems. *Ind. Eng. Chem. Fundam.* **1962**, *1*, 187–191. [CrossRef]

34. Sahu, M.; Sarkar, J. Steady-State Energetic and Exergetic Performances of Single-Phase Natural Circulation Loop With Hybrid Nanofluids. *J. Heat Transf.* **2019**, *141*, 082401. [CrossRef]

35. Animasaun, I.L.; Shah, N.A.; Wakif, A.; Mahanthesh, B.; Sivaraj, R.; Koriko, O.K. *Ratio of Momentum Diffusivity to Thermal Diffusivity: Introduction, Meta-Analysis, and Scrutinization*; Chapman and Hall: New York, NY, USA; CRC: New York, NY, USA, 2022. ISBN 9781003217374. [CrossRef]

36. Aly, E.H.; Ebaid, A. Exact Analytical Solution for Suction and Injection Flow with Thermal Enhancement of Five Nanofluids over an Isothermal Stretching Sheet with Effect of the Slip Model: A Comparative Study. *Abstr. Appl. Anal.* **2013**, *14*, 721578. [CrossRef]

37. Xiong, X.; Chen, S.; Yang, B. Natural convection of SiO_2-water nanofluid in square cavity with thermal square column. *Appl. Math. Mech.* **2017**, *38*, 585–602. [CrossRef]

38. Kandasamy, R.; Vignesh, V.; Kumar, A.; Hasan, S.H.; Isa, N.M. Thermal radiation energy due to SWCNTs on MHD nanofluid flow in the presence of seawater/water: Lie group transformation. *Ain Shams Eng. J.* **2018**, *9*, 953–963. [CrossRef]

39. Kierzenka, J.; Shampine, L.F. A BVP solver based on residual control and the Maltab PSE. *ACM Trans. Math. Softw.* **2001**, *27*, 299–316. [CrossRef]

40. Al-Mdallal, Q.M.; Syam, M.I.; Anwar, M.N. A collocation-shooting method for solving fractional boundary value problems. *Commun. Nonlinear Sci. Numer. Simul.* **2010**, *15*, 3814–3822. [CrossRef]

41. De Hoog, F.; Weiss, R. The application of Runge-Kutta schemes to singular initial value problems. *Math. Comput.* **1985**, *44*, 93–103. [CrossRef]

42. Animasaun, I.L. Significance of Quartic Autocatalysis on Fluid Flows Conveying Nanoparticles, Dust-Particles and Microstructures over an Object with Non-Uniform Thickness. Ph.D. Thesis, Federal University of Technology, Akure, Nigeria, 2019.

43. McEwen, G.F. A mathematical theory of the vertical distribution of temperature and salinity in water under the action of radiation, conduction, evaporation, and mixing due to the resulting convection. *Trans. Am. Geophys. Union* **1923**, *4*, 139. [CrossRef]

44. Flint, I.M.; Burstein, M.A. FLOTATION | Froth Processes and the Design of Column Flotation Cells. *Encycl. Sep. Sci.* **2000**, 1521–1527. [CrossRef]

45. Dey, D.; Chutia, B. Dusty nanofluid flow with bioconvection past a vertical stretching surface. *J. King Saud Univ.-Eng. Sci.* **2022**, *34*, 375–380. [CrossRef]